



# DtiStudio: Resource program for diffusion tensor computation and fiber bundle tracking

Hangyi Jiang<sup>a,b</sup>, Peter C.M. van Zijl<sup>a,b</sup>, Jinsuh Kim<sup>c,d</sup>,  
Godfrey D. Pearlson<sup>c,d</sup>, Susumu Mori<sup>a,b,\*</sup>

<sup>a</sup> Department of Radiology, Johns Hopkins University, School of Medicine, 217 Traylor Building,  
720 Rutland Avenue, Baltimore, MD 21205, United States

<sup>b</sup> F.M. Kirby Research Center for Functional Brain Imaging, Kennedy Krieger Institute, Baltimore, MD 21205, United States

<sup>c</sup> Olin Neuropsychiatry Research Center, Institute of Living, Hartford Hospital, Hartford, CT 06106, United States

<sup>d</sup> Department of Psychiatry, Yale University, School of Medicine, New Haven, CT 06510, United States

## ARTICLE INFO

### Article history:

Received 16 November 2004

Received in revised form 5 July 2005

Accepted 3 August 2005

### Keywords:

Diffusion tensor imaging

Fiber tractography

Magnetic resonance imaging (MRI)

Medical image visualization

## ABSTRACT

A versatile resource program was developed for diffusion tensor image (DTI) computation and fiber tracking. The software can read data formats from a variety of MR scanners. Tensor calculation is performed by solving an over-determined linear equation system using least square fitting. Various types of map data, such as tensor elements, eigenvalues, eigenvectors, diffusion anisotropy, diffusion constants, and color-coded orientations can be calculated. The results are visualized interactively in orthogonal views and in three-dimensional mode. Three-dimensional tract reconstruction is based on the Fiber Assignment by Continuous Tracking (FACT) algorithm and a brute-force reconstruction approach. To improve the time and memory efficiency, a rapid algorithm to perform the FACT is adopted. An index matrix for the fiber data is introduced to facilitate various types of fiber bundles selection based on approaches employing multiple regions of interest (ROIs). The program is developed using C++ and OpenGL on a Windows platform.

© 2005 Elsevier Ireland Ltd. All rights reserved.

## 1. Introduction

Diffusion tensor imaging (DTI) and DTI-based axonal mapping are becoming important tools to study brain white matter anatomy and its abnormalities [1]. However, data processing and analyses of DTI are not trivial. Unlike conventional MRI, DTI requires involved post-processing (tensor calculation) to produce images. Tensor calculation software is not readily available and data visualization and quantification are often not straightforward. **DTI calculation can produce various types of images, including apparent diffusion constant (ADC) maps, anisotropy maps, principal eigenvalue maps, eigenvector images, color maps, and so on.** In addition, three-

dimensional **tract reconstruction** based on DTI was recently introduced, which requires further computational processing [2–9]. Although this non-invasive **in vivo** method for fiber tracking is a promising technique for the understanding of human brain anatomy and functional connections, the reconstruction of neuronal projections by fiber tracking is not trivial and existing programs might be time-consuming or not user-friendly. As the importance of DTI technology in clinical practice is expected to grow in the near future, the need for resource programs that researchers and clinicians can use to rapidly process DTI data, obtain fiber tracts, and view images in three-dimensional with user-friendly interfaces, becomes paramount.

\* Corresponding author. Tel.: +1 410 614 2702; fax: +1 410 614 1948.

E-mail address: [susumu@mri.jhu.edu](mailto:susumu@mri.jhu.edu) (S. Mori).

0169-2607/\$ – see front matter © 2005 Elsevier Ireland Ltd. All rights reserved.

doi:10.1016/j.cmpb.2005.08.004

In this paper, we introduce our DTI processing and analysis software written in Visual C++ and OpenGL. The software allows users to perform DTI-related calculations, fiber tracking and editing, and ROI analysis with 3D visualization, user-friendly interface design, and memory-efficient data structure. The fiber tracking is based on the previously published Fiber Assignment by Continuous Tracking (FACT) method and brute-force fiber searching approach [2,3]. **In order to improve the computational time and memory usage, we introduced an efficient tracking algorithm and an index matrix for fiber coordinate storage.** To assure user friendliness, the application software and its components were developed on a **Windows** platform.

## 2. Theory and methods

### 2.1. DTI computation

Before tensor calculation, the Automated Image Registration (AIR) realignment procedure is performed to minimize misregistration due to subject motion [10]. In addition, the program allows the user to inspect visually the individual images and to discard the corrupted ones. This process is necessary because image corruption often occurs due to motion-related phase errors [11–14].

Most DTI acquisition sequences are based on a spin echo Stejskal–Tanner imaging sequence, in which a pair of gradient pulses is positioned around a 180° refocusing pulse for diffusion weighting [15]. The dependence of the observed echo signal intensity  $S$  on diffusion weighting is:

$$S = S_0 e^{-bD} \quad (1)$$

where  $S_0$  is the signal obtained without diffusion sensitizing gradient and  $D$  is the water diffusion constant, also known as the apparent diffusion constant (or ADC value), which can be calculated from Eq. (1) by performing a logarithmic transformation:

$$D = \text{ADC} = \frac{\ln(S/S_0)}{b} \quad (2)$$

The constant  $b$  is the diffusion-weighting factor which, for rectangular gradients, is defined by:

$$b = \gamma^2 \delta^2 G^2 \left( \Delta - \frac{\delta}{3} \right) \quad (3)$$

where  $\gamma$  is the gyromagnetic ratio,  $\delta$  and  $G$  the duration and the amplitude of the diffusion sensitizing gradient pulse along a given direction and  $\Delta$  is the time interval between the diffusion gradient pulses.

For **anisotropic** samples, Eq. (1) has to be re-written in a more general form,

$$S = S_0 e^{-b\mathbf{g}^t \mathbf{D} \mathbf{g}} = S_0 e^{-b \sum_{i,j=x,y,z} (g_i g_j) D_{ij}} \quad (4)$$

where  $\mathbf{g}$  represents the normalized diffusion sensitizing gradient vector, i.e.,  $\mathbf{g} = (g_x, g_y, g_z)^t = \mathbf{G}/|\mathbf{G}|$ .  $\mathbf{D}$  is a  $3 \times 3$  diffusion

张量是一个数学结构, 是一个椭圆形结构  
tensor in the laboratory frame,

$$\mathbf{D} = \begin{bmatrix} D_{xx} & D_{xy} & D_{xz} \\ D_{yx} & D_{yy} & D_{yz} \\ D_{zx} & D_{zy} & D_{zz} \end{bmatrix} \quad \text{其中 } D_{ij} = D_{ji}, \text{ 所以共有6个自变量} \quad (5)$$

The tensor for free diffusion (isotropic diffusion) can be visualized as a sphere, while the anisotropic diffusion of a white matter tract can be viewed as an ellipsoid. Diffusion is then faster along the principal or long axis of the ellipsoid and slower along the other two orthogonal axes. The diffusion tensor is symmetric ( $D_{ij} = D_{ji}$ , with  $i, j = x, y, z$ ) and thus has six independent variables.

Performing the natural logarithm on both sides of the Eq. (4), re-arranging the terms, and introducing the following vectors [16],

$$\bar{\mathbf{D}} = [D_{xx} \ D_{yy} \ D_{zz} \ D_{xy} \ D_{xz} \ D_{yz}]^T \quad (6)$$

and

$$\bar{\mathbf{g}} = [g_x^2 \ g_y^2 \ g_z^2 \ 2g_x g_y \ 2g_x g_z \ 2g_y g_z]^T \quad (7)$$

we have,

$$\sum_{i,j=x,y,z} (g_i g_j) D_{ij} = \bar{\mathbf{g}}^t \cdot \bar{\mathbf{D}} = \ln \frac{(S/S_0)}{b} = \text{ADC} \quad (8)$$

Because the tensor has six independent components, at least six measurements taken from different non-collinear gradient directions (and diffusion weightings if applicable) and one reference image  $S_0$  are required to determine it. By applying different gradients  $\mathbf{g}_k$  ( $k = 1, \dots, K$ ;  $K \geq 6$ ) and acquiring the corresponding signals  $S_k$ , we obtain a system of equations from which the tensor can be calculated,

$$\bar{\mathbf{g}}_k^t \cdot \bar{\mathbf{D}} = \ln \frac{(S_k/S_0)}{b_k} = \text{ADC}_k \quad (k = 1, \dots, K; K \geq 6) \quad (9)$$

This system can be rewritten compactly in matrix form:

$$\mathbf{A} \bar{\mathbf{D}} = \mathbf{B} \quad (10)$$

where  $\mathbf{A}$  is a  $K \times 6$  matrix,

$$\mathbf{A} = \begin{bmatrix} \bar{\mathbf{g}}_1^t \\ \bar{\mathbf{g}}_2^t \\ \vdots \\ \bar{\mathbf{g}}_K^t \end{bmatrix} = \begin{bmatrix} g_{1x}^2 & g_{1y}^2 & g_{1z}^2 & 2g_{1x}g_{1y} & 2g_{1x}g_{1z} & 2g_{1y}g_{1z} \\ g_{2x}^2 & g_{2y}^2 & g_{2z}^2 & 2g_{2x}g_{2y} & 2g_{2x}g_{2z} & 2g_{2y}g_{2z} \\ \vdots & \vdots & \vdots & \vdots & \vdots & \vdots \\ g_{Kx}^2 & g_{Ky}^2 & g_{Kz}^2 & 2g_{Kx}g_{Ky} & 2g_{Kx}g_{Kz} & 2g_{Ky}g_{Kz} \end{bmatrix} \quad (11)$$

and  $\mathbf{B}$  is a  $K$ -dimensional ADC vector,

$$\mathbf{B} = [\text{ADC}_1 \ \text{ADC}_2 \ \dots \ \text{ADC}_K]^T \quad (12)$$

The matrix  $\mathbf{A}$  is solely dependent on the diffusion gradient directions, while the vector  $\mathbf{B}$  is composed of ADC maps derived from each of the diffusion directions.

If at least six independent diffusion-weighted images,  $K=6$ , are acquired, the tensor can be determined uniquely. When  $K>6$ , which happens frequently in practice in order to improve signal to noise ratio and to reduce the bias of tensor estimation, Eq. (10) is over-determined [17,18]. In general, there is no solution to such an over-determined system. Instead, a best “compromise” (or fitting) solution is sought, the one that comes closest to satisfying all equations simultaneously. This is generally defined in the least-squares sense, i.e., minimizing the sum of the squares of the differences between the “true” and calculated solutions, after which this over-determined problem becomes a solvable linear least-squares problem. The solution is given by multiplying the pseudo-inverse of the matrix  $\mathbf{A}$ , denoted as  $\mathbf{A}^+$ , and vector  $\mathbf{B}$ :

$$\bar{\mathbf{D}} = \mathbf{A}^+ \mathbf{B} = (\mathbf{A}^T \mathbf{A})^{-1} \mathbf{A}^T \mathbf{B} \quad (13)$$

One of the best ways to compute  $\mathbf{A}^+$  is to use singular value decomposition [19].

## 2.2. Diffusion anisotropy calculation and visualization

From the diffusion tensor, three eigenvectors that define the direction of the diffusion system can be determined by diagonalizing the tensor for each voxel. The eigenvalues  $\lambda_1$ ,  $\lambda_2$  and  $\lambda_3$ , which correspond to the three eigenvectors, represent the magnitude of diffusivity in the three directions. Based on these three diffusivities and the mean diffusivity ( $\lambda$ ) the fractional anisotropy (FA) was calculated to yield values between 0 and 1:

$$FA = \frac{\sqrt{3}}{\sqrt{2}} \frac{\sqrt{(\lambda_1 - \lambda)^2 + (\lambda_2 - \lambda)^2 + (\lambda_3 - \lambda)^2}}{\sqrt{\lambda_1^2 + \lambda_2^2 + \lambda_3^2}} \quad (14)$$

where

$$\lambda = \frac{\lambda_1 + \lambda_2 + \lambda_3}{3} \quad (15)$$

It is clear from this definition that fully anisotropic tissues ( $\lambda_1 > 0$ ,  $\lambda_2 = \lambda_3 = 0$ ) have  $FA = 1$ , while fully isotropic tissues ( $\lambda_1 = \lambda_2 = \lambda_3$ ) have  $FA = 0$ .

Two other commonly used anisotropy definitions are the relative anisotropy (RA) and the volume ratio (VR), defined, respectively, as [20]:

$$RA = \frac{\sqrt{3}}{\sqrt{2}} \frac{\sqrt{(\lambda_1 - \lambda)^2 + (\lambda_2 - \lambda)^2 + (\lambda_3 - \lambda)^2}}{\lambda_1 + \lambda_2 + \lambda_3} \quad (16)$$

$$VR = 1 - \frac{\lambda_1 \lambda_2 \lambda_3}{\lambda^3} \quad (17)$$

In addition, the following measures of anisotropy calculations are supported.

$$FA_{i,j} = \frac{\sqrt{2} \sqrt{(\lambda_i - (\lambda_i + \lambda_j)/2)^2 + (\lambda_j - (\lambda_i + \lambda_j)/2)^2}}{\sqrt{\lambda_i^2 + \lambda_j^2}} \quad (i, j = 1, 2, 3) \quad (18)$$

and the spherical diffusion variance (SDV) defined as [21]:

$$SDV = \sqrt{\frac{1}{K} \sum_{k=1}^K (ADC_k - ADC_{mean})^2} \quad (K \geq 6) \quad (19)$$

where  $ADC_{mean}$  denotes the average over all calculated ADC maps. The SDV image is not based on tensor calculation.

Anisotropy images only show the magnitude of the anisotropy. Because the direction of the principal eigenvector is also important, color mapping is widely used, in which information regarding orientation (color) is combined with information on anisotropy (image intensity). For color coding, the principal eigenvector is projected into three different directions (to different color components) in the image reference frame using:

$$(r, g, b) = FA \cdot (v_x, v_y, v_z) \quad (20)$$

where  $r$ ,  $g$ , and  $b$  represent red, green and blue components of the voxel color, and  $(v_x, v_y, v_z)$  is the normalized principal eigenvector, which is associated with the largest eigenvalues. In this equation, FA was used for intensity weighting and  $(v_x, v_y, v_z)$  for color coding. The software has a choice to use any anisotropy map for the intensity weighting and secondary or tertiary eigenvector for the color coding.

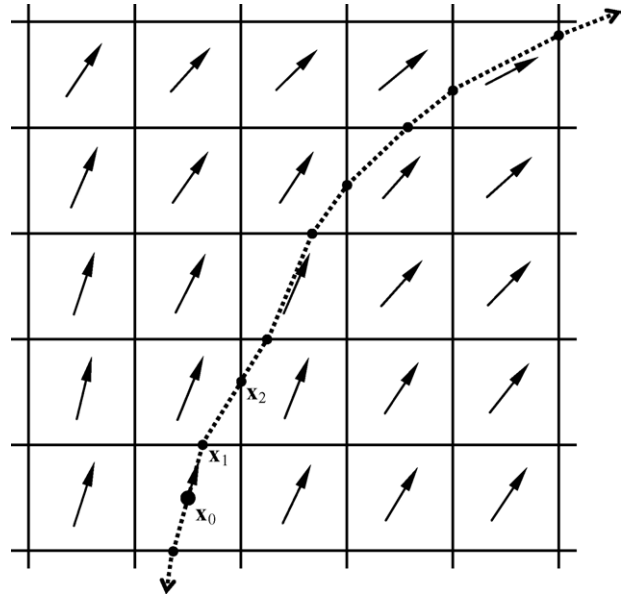


**Fig. 1 – Illustration of fiber tracking algorithm.** The black arrows are principal eigenvectors which correspond to the longest axis of the diffusion ellipsoid. The dashed route is the tracked fiber tract. The tracking starts from the seed point  $x_0$ , which has a FA value bigger than the threshold. While moving along the eigenvector direction, the tract hits the boundary of the voxel at point  $x_1$ . At this point, the tracking direction is changed to that of the new voxel. Adapting this strategy iteratively in both directions starting from the seed point, a continuous fiber trajectory can be obtained. The tracking is stopped when FA is lower than the threshold or the angle between two eigenvectors to be connected is greater than a threshold (sharp turn); the thresholds are user definable in the program.

两种搜索方法：单跟踪、强力搜索法

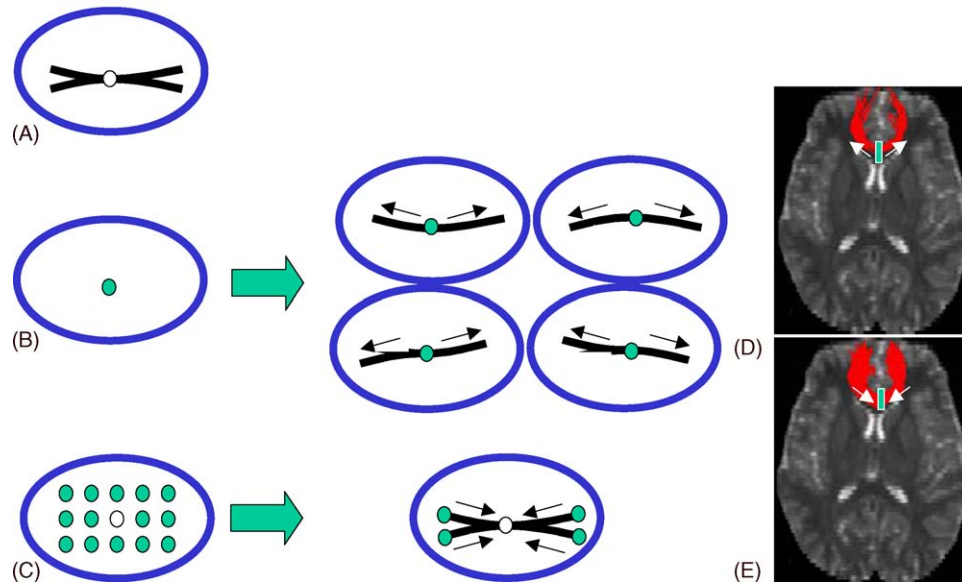


Fig. 2 – Schematic diagram of the difference between the single tracking (B) and brute-force search approaches (C). Suppose (A) represents the shape of a white matter tract of interest with an anatomical landmark indicated by a white circle. If a tracking is initiated from the landmark, there are four possibilities for the results, each representing one branch of the tract (B). This is because a propagation result from one pixel can delineate only one line. Conversely, the line propagation can be initiated from all pixels and all propagation results that penetrate the anatomical landmark are searched, which leads to more comprehensive delineation of the tract of interest. Images in (D and E) compare the tracking results by conventional (D) and brute-force approach (E) for the genu of the corpus callosum.

### 2.3. Fiber tracking

DTI provides a unique tool for investigating brain structures and for assessing axonal fiber architectures in vivo. The fiber-tracking algorithm is based on the Fiber Assignment by Continuous Tracking (FACT) approach, by which tracking is performed using a continuous coordinate system rather than a discrete voxel-based matrix grid (see Fig. 1) [2,3]. The fiber tracking is started at the center of each voxel having a fractional anisotropy (FA) value greater than a user-defined threshold, and proceeds along the principal eigenvector direction. At the point where the track intercepts the voxel's boundary, the tracking direction is changed to that of its neighbor. Applying this tactic iteratively, a continuous fiber trajectory can be obtained. Tracking is stopped at voxels where FA is lower than the threshold (FA threshold) or where the angle

between two eigenvectors to be connected by the tracking is greater than a user-defined threshold (angle threshold).

One challenge is how to find the interception point of the three-dimension axonal tract and the boundary of the voxel as efficiently as possible. To get the appropriate answer, the 3D-space fiber track within the voxel is parameterized by its arc length,  $s$ , and expressed as a set of linear parameter functions:

$$\begin{cases} x = x_0 + v_x s \\ y = y_0 + v_y s \\ z = z_0 + v_z s \end{cases} \quad (21)$$

where  $\mathbf{v} = (v_x, v_y, v_z)$  is the principal eigenvector,  $\mathbf{x}_0 = (x_0, y_0, z_0)$  is the starting point where the fiber track enters the voxel and  $\mathbf{x} = (x, y, z)$  is the interception point where the fiber

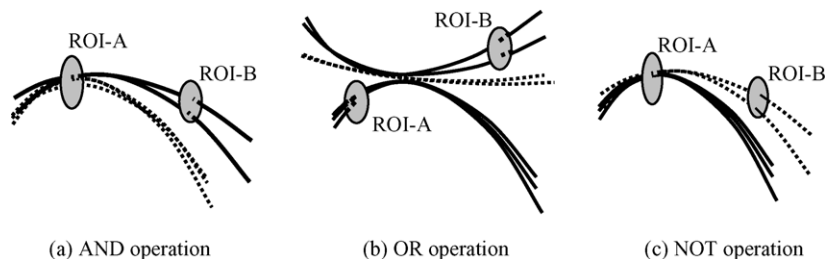


Fig. 3 – Fiber trajectories selection using multiple ROIs. The selected fiber tracts are shown in solid lines. The operations are named AND, OR, and NOT, respectively. If ROI-A was defined first and ROI-B second, then (a) AND operation will restrict the fibers to those that penetrate both ROI-A and ROI-B; (b) OR operation will select fibers passing through either ROI-A or ROI-B; (c) NOT operation, will remove a subset of fibers that pass through ROI-B.



track leaves the current voxel and enters the next. The surfaces of the cube-shaped voxel can be described as a set of 3D-planes that are equated with  $x$ ,  $y$ , or  $z$  being the constants. Tracking from  $\mathbf{x}_0$  along the direction  $\mathbf{v}$  by increasing parameter  $s$ , the track will hit the cube-boundary at the point where at least one of its  $x$ ,  $y$ , or  $z$  components becomes a constant. Thus, the minimum  $s$  that makes  $x$ ,  $y$ , or  $z$  in this equation a constant number is the expected solution for the interception point of the tract and the cube surface. Another problem that needs to be addressed here is how to assign the direction of the eigenvector consistently, since its sign can be positive or negative. To decide the direction of the new vector to be connected by tracking, an inner product between it and the present vector is carried out. If the result is positive, we keep the sign of the new eigenvector, otherwise, we swap its sign. Tracking is implemented in both forward and backward directions initiated from the seed point to get a complete fiber trajectory. A minimum fiber length testing is subsequently performed on the fiber chain to remove tracts shorter than a user-defined threshold. For visualization, 3D-interpolation and smoothing were implemented on the jagged tract followed by the continuous tracking, resulting in an equally sampled and smoothed 3D curve.

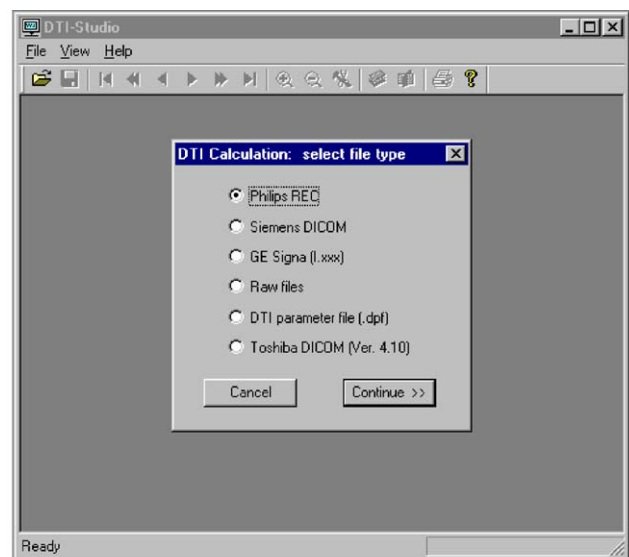
Fiber tracking could start by identifying an anatomical landmark and drawing a region of interest (ROI). The problem with this approach, however, is that whenever the tracking meets a branching point, it would be forced to follow only one of them. In other words, the number of tracts yielded by this technique would not be more than the number of pixels in a ROI. To remedy this unwanted situation, **brute-force** fiber tracking is adopted in our work by tracking from every single voxel in the whole 3D-image data set, after which the trajectories passing through the ROI are identified [4,22,9]. This approach leads to more comprehensive branching-patterns of the fiber bundles. These bundles include not only the fibers that started from the ROI points but also from other seed points where the tracking leads to the ROI, which may suggest the branching or merging of the tracts (Fig. 2).

The brute-force tracking results in a large amount of coordinate data. For example, a typical DW-image matrix, size of  $256 \times 256 \times 50$ , yields more than 200,000 fiber tracts (with FA threshold 0.4 and tract-turning angle threshold  $70^\circ$ ). **These tracts must be stored in a way that is both memory and operation efficient, so that the process of searching or labeling fiber bundles penetrating a ROI is easier and quicker.** To address this question, an index matrix with the same size as the original image is introduced in which each voxel holds the pointers to the fiber data chains passing through this voxel. In this way, identifying the fiber chains associated with any voxels becomes straightforward and efficient. Additionally, an attribute table is kept with each fiber chain in which visualization features, such as fiber color and labeling status, are stored.

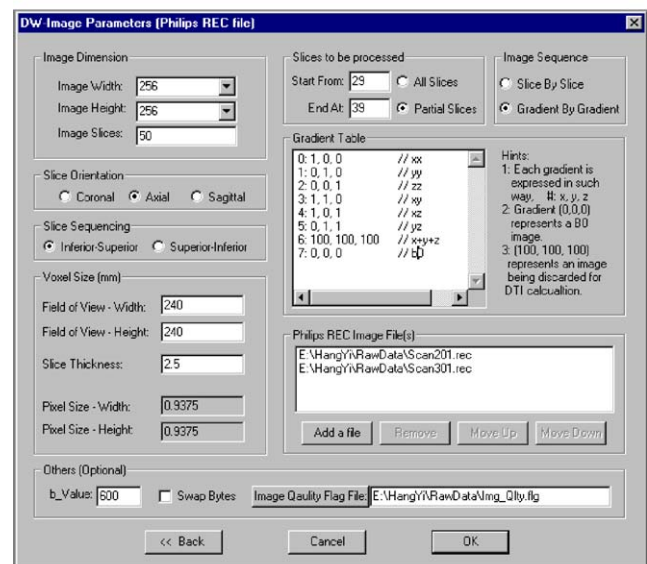
**In summary, the tracking algorithm can be described as follows:**

1. Start from a seed point  $\mathbf{x}_0$  with FA value greater than the set threshold.

2. Take the eigenvector  $\mathbf{v}$  at  $\mathbf{x}_0$  as the current direction.
3. Find out the interception point  $\mathbf{x}$  of the track on the boundary of the voxel by Eq. (21), where  $s$  is minimal.
4. If the tract hits the boundary of the image block, go to step 9.
5. If FA of the new voxel associated with  $\mathbf{x}$  is less than the threshold, go to step 9.
6. Get inner product between current and new eigenvectors, swap sign of new vector if the result is negative.
7. If the angle between current direction  $\mathbf{v}$  and new direction associated with  $\mathbf{x}$  is greater than the set threshold, go to 9.
8. Assign  $\mathbf{x}$  to  $\mathbf{x}_0$ , and go to step 2.



(a)



(b)

**Fig. 4 – Interfaces to import image files and parameters. First, manufacturer of the source data is specified (a). In a subsequent window (b), various imaging parameters and filenames are specified.**

9. Restart from the original seed point  $\mathbf{x}_0$ , swap the eigenvector  $\mathbf{v}$  at  $\mathbf{x}_0$ , perform tracking in reverse direction from step 2 again. If tracking has been completed for both directions, proceed to next step.
10. Combine the tracking results of both directions from seed point together to produce a fiber coordinate chain. If it passes the minimum fiber length test, then perform 3D-curve interpolation and smoothing and create an attribute table with this fiber chain.
11. Apply 1–10 iteratively, until the complete image is processed.
12. Create an index matrix with the same size of the original image, in which each voxel stores the pointers to the fiber chains that penetrate this voxel.

#### 2.4. Fiber data manipulation

The purpose of fiber data manipulation is to interactively select axonal fibers passing through user-defined ROIs. Taking advantage of the index matrix associated with the fiber coordinate chains, it is straightforward to label the tracts of interest penetrating a ROI. When multiple ROIs are used, we use three kinds of ROI-based Boolean operations that enable the fiber selections to be flexible and versatile [4,23,7]. These operations are: AND (intersection), OR (union), and NOT (exclusion). The choice of operation depends on the characteristic trajectory of each tract. As shown in Fig. 3, if ROI-A was drawn first and ROI-B next, the use of the AND operation will result in the tracts going through both ROI-A and ROI-B (restrict the fibers of

ROI-A passing through ROI-B). The OR operation, on the other hand, will produce fibers passing through either ROI-A or ROI-B (add more tracts on the results of ROI-A). The NOT operation results in the fibers penetrating ROI-A but not ROI-B (remove a subset from projections from construction results of ROI-A). These operations can be employed sequentially to select the tract pathways of interest.

### 3. Implementation and results

The program has been developed on the Windows platform with user-friendly interface design (Fig. 4). It follows the Windows-style convention for buttons and menus. Currently, data formats of Philips, GE, Siemens, and Toshiba scanners, DICOM and raw data matrix with user-specified header are supported. The gradient orientation table,  $b$ -values, and other imaging parameters needed for the tensor calculation are also specified in this window. Alternatively, these parameters can be specified in an ASCII file (called dpf file—DTI parameter file) and then fed into the program.

The unlimited number of gradient orientations can be specified in a gradient table window (Fig. 4(b)). Because of occasional image corruption and subject motions (co-registration error), users are not encouraged to perform signal averaging by a scanner, but to acquire multiple redundant datasets which are stored separately in image files. These multiple files can be listed in this dialog window or in the dpf file so that the software can read all images simultaneously.

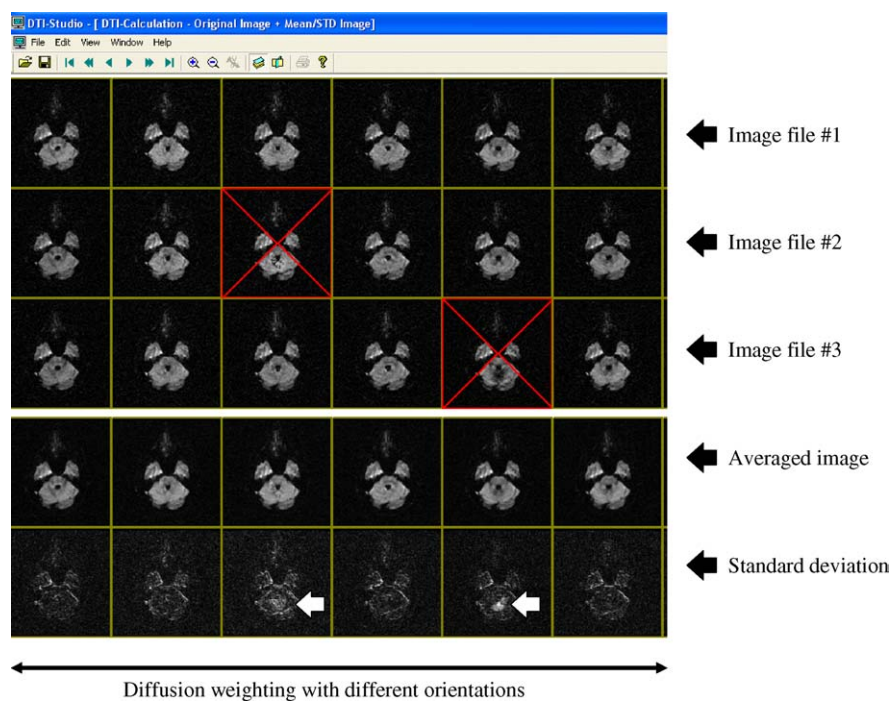


**Fig. 5 – A screen shot to inspect image quality. Before DTI calculation, all individual images are visually inspected to **discard corrupted images** from the subsequent least mean-square fitting. In this example, there are three repeated scans. By clicking the corrupted images, these are crossed out as shown in the figure. The three redundant datasets (rather than signal averaging by the scanner), provides a visual clue to judge the image quality. To further assist the inspection, mean and standard deviation images can be displayed. Contamination of corrupted images is manifested by bright standard deviation images (white arrows).**

### 3.1. DTI calculation

The following steps are adopted for diffusion tensor image computation:

1. As an option, image co-registration is performed to remove small bulk motions that occurred during the scans. This procedure is based on AIR.
2. Read data from various platforms (see Fig. 4).
3. Perform image quality inspection visually using the image inspection window. This window allows users to discard the corrupted images before the subsequent computations

(as shown in Fig. 5). The judgment of image quality is based on visual inspection. This window has several features to help this inspection. First, images from repeated measurements are displayed together. Because these images are acquired with the same imaging parameters, they should look identical (Fig. 5, image files #1–3). Second, average and standard deviation images of the repeated measurements can be displayed. If there is a large amount of fluctuation in imaging quality, it is detected by bright standard deviation images (Fig. 5, white arrows). This window is also useful to examine the quality of image co-registration. If slice levels of the three redundant images are not identical, the AIR-

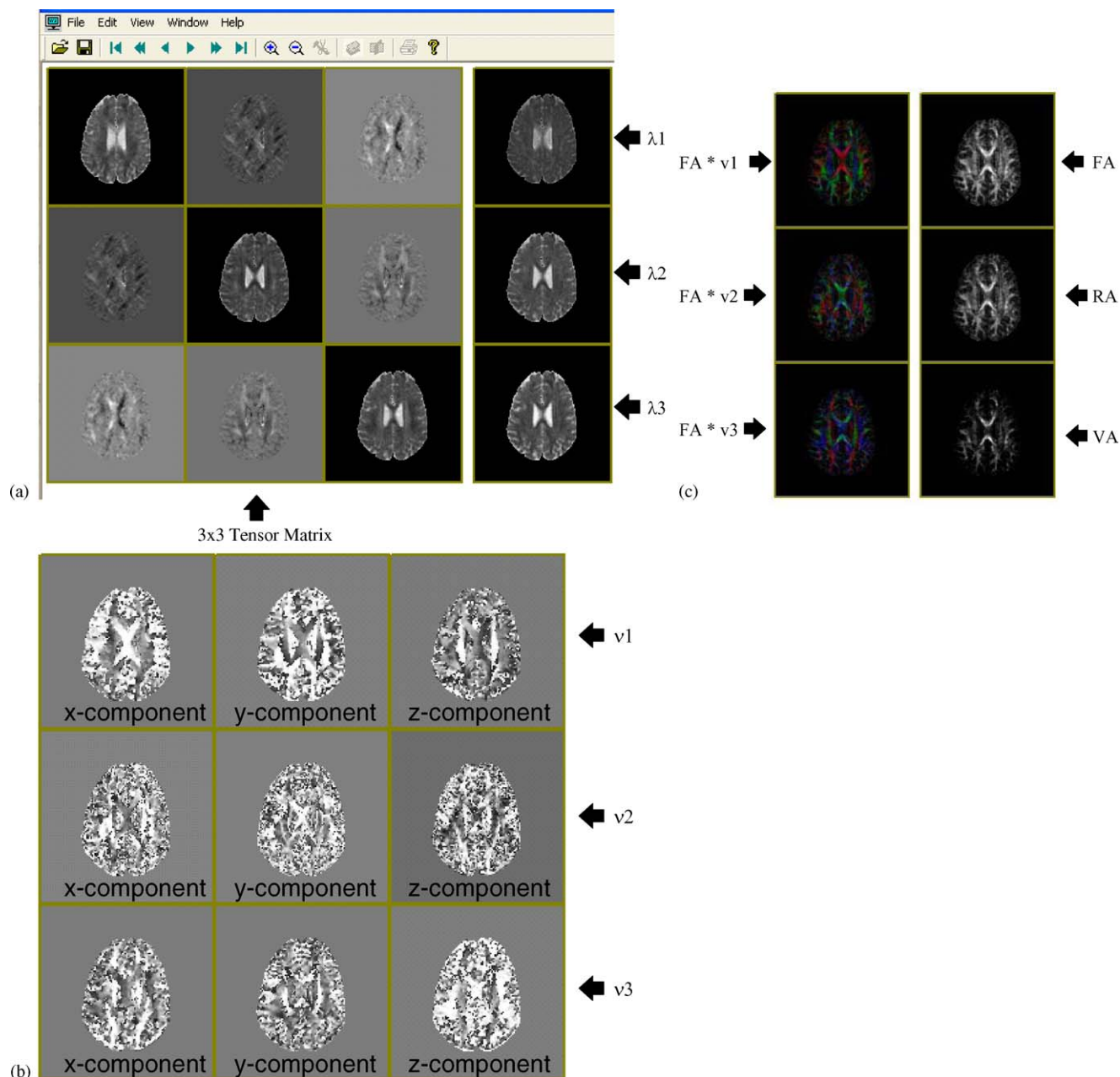
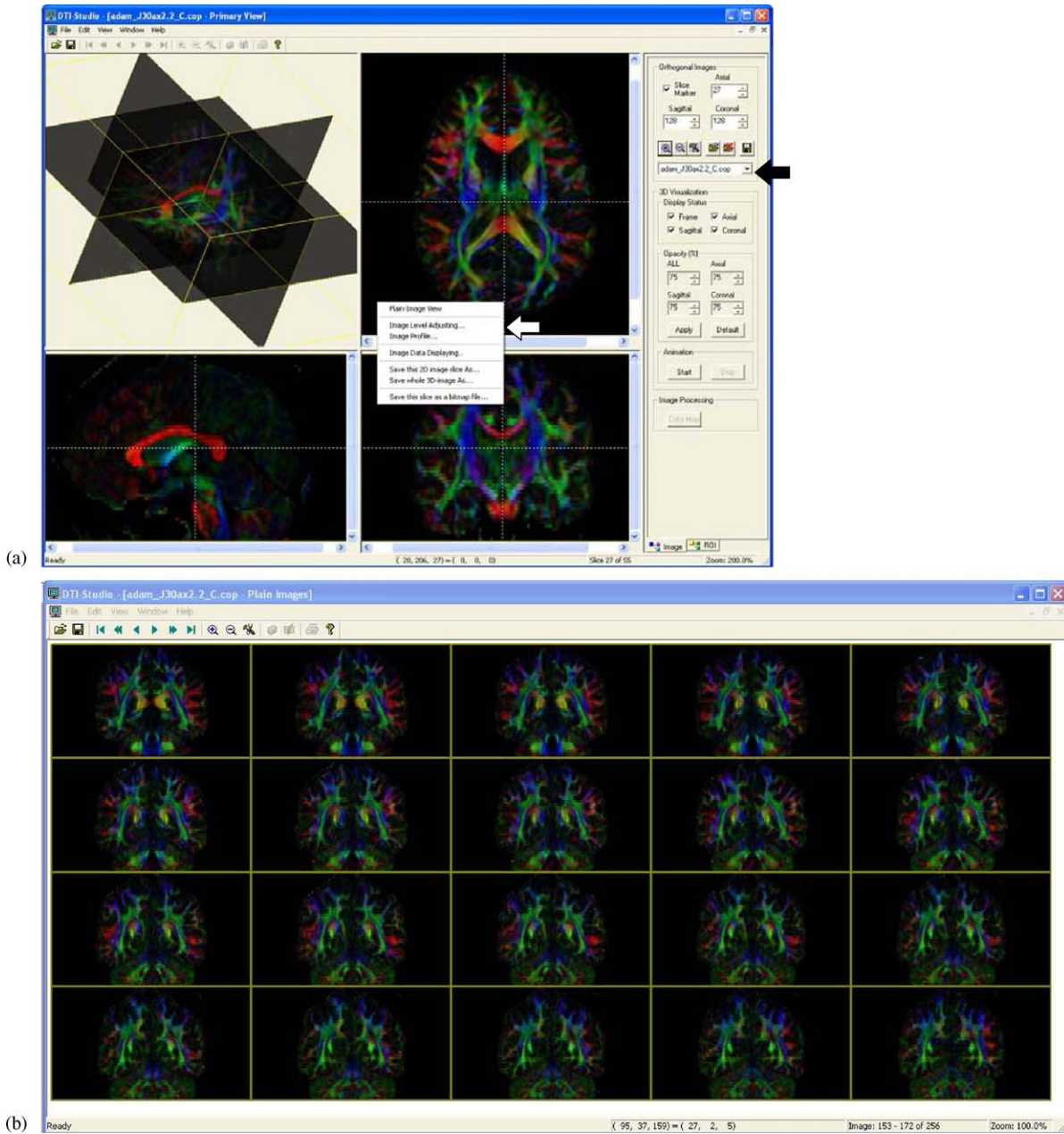


Fig. 6 – Screen shots demonstrating the program for DTI calculation. The results are shown as a plain-view mode. In (a) the tensor is presented as a  $3 \times 3$  image matrix, with the images arranged as if positioned inside the tensor. Three eigenvalue images ( $\lambda_1$ – $\lambda_3$ ) are also displayed. (b) Three eigenvector images ( $v_1$ – $v_3$ ). (c) Color-coded orientation maps (first column) and three types of anisotropy maps (FA, VA, and RA). All these images can also be visualized by a tri-planar viewer shown in Fig. 7 and values can be quantified for each pixel or by ROI drawing.





**Fig. 7 – Windows for interactive visualization of various contrasts created after tensor calculation. The three 2D orthogonal views can be controlled by mouse or directly specifying slice numbers (a). The 3D tri-planar view shows three slices corresponding to the selected 2D slices three dimensionally. Transparency of the slices can be individually controlled. A pull-down menu (black arrow) allows the user to load various types of images obtained from the tensor calculations, as well as raw diffusion-weighted images. From a contextual menu (right mouse click), contrast/brightness can be controlled or images can be exported as a file (white arrow). The menu also allows the user to switch to the plain image view (b) of the selected slice orientations (axial, coronal, or sagittal).**

based co-registration should be performed (step 1). Slight mis-registration manifests as bright edges in the standard deviation maps as can be seen in Fig. 5. If the signal is averaged in a scanner, this type of quality check and corrections cannot be performed.

4. For each image slice, calculate the over-determined matrix  $A$  and the ADC vector  $B$  for the corresponding DTI scheme using Eqs. (11) and (12).

5. Determine the pseudo-inverse of the matrix  $A$  using singular value decomposition and compute the tensor for each pixel based on Eq. (13).

Once the calculation is finished, tensor element images are displayed as shown in Fig. 6. The data used in this figure is a  $256 \times 256 \times 55$  dataset obtained with 15 gradient directions in addition to one  $b=0$  image. The processing time is less than



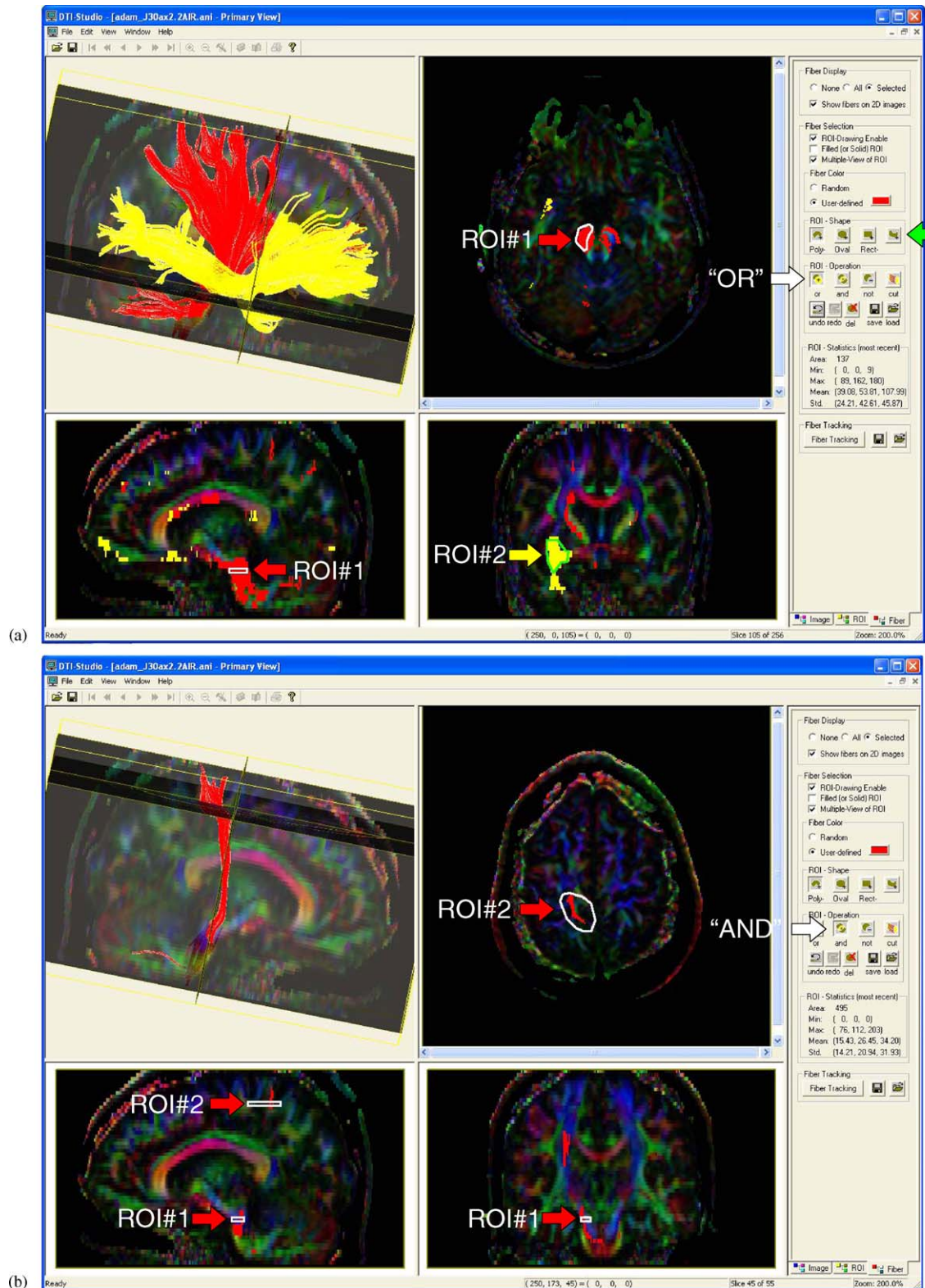


**Fig. 8 – Examples of 3D fiber tracking results, visualization, and fiber editing. (a) Three types of ROI drawing tools (polygon, oval, and rectangle) are available now (green arrow). As soon as an ROI is drawn, fibers that penetrate it are retrieved from memory and shown by a color defined by the user. The fiber trajectories are shown both in three 2D orthogonal views and the 3D tri-planar view. For multiple ROI approaches, three types of operations (OR, AND and NOT) are supported (white arrow). In this example, projection fibers (red) and inferior fronto-occipital fasciculus (yellow) are visualized using OR operation. (b) An example of AND operation, in which only the motor pathway was visualized by defining the second ROI at the precentral gyrus. (For interpretation of the references to color in this figure legend, the reader is referred to the web version of this article.)**

1 min (Windows-XP, Pentium IV, 2 GHz, 1 GB RAM). We are routinely performing 30-orientation measurements with five  $b=0$  images with the same matrix size, which takes less than 3 min to complete the DTI calculation.

From the tensor elements, various images are calculated and ready for visualization. Fig. 7 shows one of the viewing windows (2D and tri-planar viewer). From a pull-down list, a contrast of interest can be selected and viewed. These include various types of anisotropy maps and color-coded maps as described in the last section, as well as raw diffusion-weighted images and result images presented in Fig. 6. The visualization includes three orthogonal 2D views (coronal, axial, and sagittal) and a 3D tri-planar view. Images can be magnified or shrunk, and interactively manipulated.

### 3.2. Fiber tracking

Before tracking is performed, a window is displayed to specify the two thresholds (FA and angle thresholds) for tracking. Tracking is performed from all pixels, in which FA values are higher than the threshold. For a typical  $256 \times 256 \times 50$  image matrix, as shown in Fig. 7, using default thresholds (FA > 0.2 and tract-turning angle < 40°), more than 570,000 fiber tracts are found with average length of 31 pixels and maximum length of 394 pixels (without interpolation). Of the voxels that the tracts passing through, the average number of fibers per voxel is 4.1, while the maximum number is up to 681. This tracking procedure uses less than 3 min.

Results of the tracking can be displayed in the same three 2D orthogonal and 3D tri-plane views, or a series of 2D slices (Fig. 7(b)). Because of the sheer number of the fiber tracts reconstructed by the brute-force approach, fibers are usually visualized only after a ROI is drawn. Namely, in subsequent fiber visualization processes, tracking is no longer performed and only the fibers of interest that penetrate ROIs are shown, which allows real-time fiber-editing. Fig. 8(a) shows an example in which projection fibers that penetrate the cerebral peduncle (ROI #1) and the inferior fronto-occipital fasciculus (ROI #2) are both visualized with different color assignment using OR operation. Fig. 8(b) shows an example of AND operation, in which the second ROI (ROI #2) was drawn near the precentral gyrus to identify trajectories from the cerebral peduncle (ROI #1). This result should contain a high concentration of fibers from the motor pathway. The user can rotate, zoom in/out, or shift on the 2D and 3D view interactively by using mouse or keyboard.

The tracking results can be saved and loaded using a designed compact format.

## 4. Discussion and conclusion

### 4.1. Applications and limitations of fiber tracking

Diffusion tensor imaging is unique in its ability to quantify changes in neural tissue microstructure within the human brain non-invasively. DTI-based tractography should improve our understanding of brain pathology, particularly of white matter abnormalities occurring in head trauma, stroke, etc. Fiber tractography methods could be applied to other soft

fibrous tissues, such as muscles, tendons, heart, etc., whose fiber directional pattern and organization is critical in following its normal development and diagnosing disease.

Although the DTI-based fiber reconstruction technique is a powerful technique, its limitations should be discussed. First, the DTI-based tracking technique, which is based on water movement, cannot distinguish orthograde and retrograde directions of axonal tracts. Second, image resolution for a typical human DTI study is on the order of 1–5 mm. Once an axon of interest enters a pixel of this size and mixes with other axons of different destinations, information about cellular level connectivity degenerates. Therefore, cellular-level connectivity cannot be found by this technique. It should always be kept in mind that the eigenvector derived from the diffusion tensor is actually a voxel-averaged measurement. Therefore, the principal eigenvector only corresponds to the average fiber direction within the voxel. Thus, DTI can reveal only macroscopic architecture of the white matter.

### 4.2. Concluding remarks

A user-friendly DTI processing, analysis, and visualization software was developed. Processing includes image quality inspection, and DTI calculation that will yield ADC maps, tensor maps, color maps, isotropic images, anisotropy measurements, eigenvalue and eigenvector images. Visualization was implemented in 2D orthogonal and 3D tri-planar views. Efficient fiber tracking was developed as a part of the analysis tools. A rapid algorithm to perform CPU-intensive brute-force fiber tracking and memory-efficient fiber coordinate storage were developed and employed. The program has been successfully adapted to various sources of data. The software is available at <http://mri.kennedykrieger.org/sitemap/software.htm>.

## Acknowledgments

This study was supported in part by NCRR resource grant P41 RR15241 (SM, PVZ). Dr. van Zijl is a paid lecturer for Philips Medical Systems. This arrangement has been approved by Johns Hopkins University in accordance with its conflict of interest policies.

## REFERENCES

- [1] P.J. Basser, J. Mattiello, D. LeBihan, Estimation of the effective self-diffusion tensor from the NMR spin echo, *J. Magn. Reson. B* 103 (1994) 247–254.
- [2] S. Mori, B.J. Crain, V.P. Chacko, P.C.M. van Zijl, Three-dimensional tracking of axonal projections in the brain by magnetic resonance imaging, *Ann. Neurol.* 45 (2) (1999) 265–269.
- [3] R. Xue, P.C.M. van Zijl, B.J. Crain, M. Solaiyappan, S. Mori, In vivo three-dimensional reconstruction of rat brain axonal projections by diffusion tensor imaging, *Magn. Reson. Med.* 42 (6) (1999) 1123–1127.
- [4] T.E. Conturo, N.F. Lori, T.S. Cull, E. Akbudak, A.Z. Snyder, J.S. Shimony, R.C. McKinstry, H. Burton, M.E. Raichle, Tracking neuronal fiber pathways in the living human

- brain, *Proc. Natl. Acad. Sci. U.S.A. Appl. Phys. Sci., Neurobiol.* 96 (18) (1999) 10422–10427.
- [5] D.K. Jones, A. Simmons, S.C.R. Williams, M.A. Horsfield, Non-invasive assessment of axonal fiber connectivity in the human brain via diffusion tensor MRI, *Magn. Reson. Med.* 42 (1) (1999) 37–41.
  - [6] P.J. Basser, S. Pajevic, C. Pierpaoli, J. Duda, A. Aldroubi, In vivo fiber tractography using DT-MRI data, *Magn. Reson. Med.* 44 (4) (2000) 625–632.
  - [7] S. Mori, W. Kaufmann, C. Davatzikos, B. Stieltjes, L. Amodi, K. Fredericksen, G. Pearlson, E. Melhem, M. Solaiyappan, G. Raymond, H. Moser, P. van Zijl, Imaging cortical association tracts in the human brain using diffusion-tensor-based axonal tracking, *Magn. Reson. Med.* 47 (2) (2002) 215–223.
  - [8] C. Poupon, C.A. Clark, V. Frouin, J. Regis, I. Bloch, D. Le Bihan, J.-F. Mangin, Regularization of diffusion-based direction maps for the tracking of brain white matter fascicles, *NeuroImage* 12 (2) (2000) 184–195.
  - [9] B. Stieltjes, W.E. Kaufmann, P.C.M. van Zijl, K. Fredericksen, G.D. Pearlson, M. Solaiyappan, S. Mori, Diffusion tensor imaging and axonal tracking in the human brainstem, *NeuroImage* 14 (2001) 723–735.
  - [10] R.P. Woods, S.T. Grafton, C.J. Holmes, S.R. Cherry, J.C. Mazziotta, Automated image registration. I. General methods and intrasubject, intramodality validation, *J. Comput. Assist. Tomogr.* 22 (1998) 139–152.
  - [11] R.J. Ordidge, J.A. Helpert, Z.X. Qing, R.A. Knight, V. Nagesh, Correction of motional artifacts in diffusion-weighted NMR images using navigator echoes, *Magn. Reson. Imag.* 12 (1994) 455–460.
  - [12] K. Butts, A. de Crespigny, J.M. Pauly, M. Moseley, Diffusion-weighted interleaved echo-planar imaging with a pair of orthogonal navigator echoes, *Magn. Reson. Med.* 35 (1996) 763–770.
  - [13] D.G. Norris, Implications of bulk motion for diffusion-weighted imaging experiments: effects, mechanisms, and solutions, *J. Magn. Reson. Imag.* 13 (2001) 486–495.
  - [14] H. Jiang, X. Golay, P.C.M. van Zijl, S. Mori, Origin and minimization of residual motion-related artifacts in navigator-corrected segmented diffusion-weighted EPI of the human brain, *Magn. Reson. Med.* 47 (4) (2002) 818–822.
  - [15] E.O. Stejskal, J.E. Tanner, Spin diffusion measurements: spin echoes in the presence of a time-dependent field gradient, *J. Chem. Phys.* 42 (1965) 184–195.
  - [16] P.J. Basser, J. Mattiello, D. LeBihan, MR diffusion tensor spectroscopy and imaging, *Biophys. J.* 66 (1) (1994) 259–267.
  - [17] D.K. Jones, M.A. Horsfield, A. Simmons, Optimal strategies for measuring diffusion in anisotropic systems by magnetic resonance imaging, *Magn. Reson. Med.* 42 (3) (1999) 515–525.
  - [18] S. Skare, M. Hedehus, M.E. Moseley, T.-Q. Li, Condition number as a measure of noise performance of diffusion tensor data acquisition schemes with MRI, *NeuroImage* 147 (2000) 340–352.
  - [19] W.H. Press, S.A. Teukolsky, W.T. Vetterling, B.P. Flannery, *Numerical Recipes in C*, Cambridge University Press, 1992.
  - [20] C. Pierpaoli, P.J. Basser, Toward a quantitative assessment of diffusion anisotropy, *Magn. Reson. Med.* 36 (1996) 893–906.
  - [21] L.R. Frank, Anisotropy in high angular resolution diffusion-weighted MRI, *Magn. Reson. Med.* 45 (2001) 935–939.
  - [22] D.J. Werring, A.T. Toosy, C.A. Clark, G.J. Parker, G.J. Barker, D.H. Miller, A.J. Thompson, Diffusion tensor imaging can detect and quantify corticospinal tract degeneration after stroke, *J. Neurol. Neurosurg. Psychiatry* 69 (2000) 269–272.
  - [23] M. Catani, R.J. Howard, S. Pajevic, D.K. Jones, Virtual in vivo interactive dissection of white matter fasciculi in the human brain, *NeuroImage* 17 (2002) 77–94.